Theoret. Comput. Fluid Dynamics (1996) 8: 325–347

Theoretical and Computational Fluid Dynamics

Görtler Vortices with System Rotation[1]

Alessandro Bottaro, Barbro G.B. Klingmann,[2] and Abdelfattah Zebib[3]

IMHEF-DGM, Ecole Polytechnique Fédérale de Lausanne, CH-1015 Lausanne, Switzerland

Communicated by P. Hall

Received 15 February 1995 and accepted 7 September 1995

Abstract. The steady primary instability of Görtler vortices developing along a curved Blasius boundary layer subject to spanwise system rotation is analysed through linear and nonlinear approaches, to clarify issues of vortex growth and wavelength selection, and to pave the way to further secondary instability studies.

A linear marching stability analysis is carried out for a range of rotation numbers, to yield the (predictable) result that positive rotation, that is rotation in the sense of the basic flow, enhances the vortex development, while negative rotation dampens the vortices. Comparisons are also made with local, nonparallel linear stability results (Zebib and Bottaro, 1993) to demonstrate how the local theory overestimates vortex growth. The linear marching code is then used as a tool to predict wavelength selection of vortices, based on a criterion of maximum linear amplification.

Nonlinear finite volume numerical simulations are performed for a series of spanwise wave numbers and rotation numbers. It is shown that energy growths of linear marching solutions coincide with those of nonlinear spatially developing flows up to fairly large disturbance amplitudes. The perturbation energy saturates at some downstream position at a level which seems to be independent of rotation, but that increases with the spanwise wavelength. Nonlinear simulations performed in a long (along the span) cross section, under conditions of random inflow disturbances, demonstrate that: (i) vortices are randomly spaced and at different stages of growth in each cross section; (ii) "upright" vortices are the exception in a universe of irregular structures; (iii) the average nonlinear wavelengths for different inlet random noises are close to those of maximum growth from the linear theory; (iv) perturbation energies decrease initially in a linear filtering phase (which does not depend on rotation, but is a function of the inlet noise distribution) until coherent patches of vorticity near the wall emerge and can be amplified by the instability mechanism; (v) the linear filter represents the *receptivity* of the flow: any random noise, no matter how strong, organizes itself linearly before subsequent growth can take place; (vi) the Görtler number, by itself, is not sufficient to define the state of development of a vortical flow, but should be coupled to a receptivity parameter; (vii) randomly excited Görtler vortices resemble and scale like coherent structures of turbulent boundary layers.

[1] A.Z. has been supported, during his stay at EPFL, by an ERCOFTAC Visitor Grant. A.B. acknowledges the Swiss National Fund, Grant No. 21-36035.92, for travel support associated with this research. This work was also supported by the Swedish Board of Technical Development (NUTEK), the Swedish Technical-Scientific Council (TFR), and an ERCOFTAC Visitor Grant, through which the stay of B.G.B.K. at the EPFL was made possible. Cray-2 computing time for this research was generously provided by the Service Informatique Centrale of EPFL.

[2] Present address: Volvo Aerospace Corp., Space Propulsion Division, S-461 81 Trollhättan, Sweden.

[3] Permanent address: Rutgers University, Mechanical and Aerospace Engineering, Piscataway, NJ 08855-0909, U.S.A.

1. Introduction

The subject of this work is the spatial development of the boundary-layer flow over a concave surface subject to system rotation, with the axis of rotation perpendicular to the plane of the base motion. Applications of the present problem include, for example, the flow along pressure surfaces of rotating blades, where the combined effects of pressure gradients, curvature, and rotation determine the flow character and its stability. Interest in vortices developing along curved boundary layers stems also from their similarities with coherent structures in the near-wall region of turbulent shear flows (Blackwelder, 1983). Streamwise vortices can also be excited in a flat-plate boundary layer by an algebraic instability (Landahl, 1980; Trefethen *et al.*, 1993), and in fact streamwise or quasi-streamwise vortices constitute the *optimal perturbation* (the perturbation with the largest initial transient amplification (Butler and Farrel, 1992)) for the Blasius flow. Vortices in nonrotating curved boundary layers have been the subject of renewed studies in recent years to understand issues of wavelength selection and the onset of secondary, time-dependent motions. The experiments of Swearingen and Blackwelder (1987), henceforth referred to as SB, have provided a basis for the computational studies of, among others, Lee and Liu (1992) and Guo and Finlay (1994). While these computations have faithfully reproduced laboratory results when experimentally established initial and boundary conditions are used, only theory (Floryan and Saric, 1984; Guo and Finlay, 1994) has provided some criteria for the wavelength selection. It has been argued that a wavelength in the neighborhood of the curve of maximum linear amplification has a good chance of being selectively amplified. This has been confirmed in experiments where the upstream flow perturbations are randomly distributed along the span, but it is at variance with other experimental evidence that indicates that different wavelengths are selected in different experiments (compare, e.g., Tani, 1962; Bippes and Görtler, 1972; Bippes, 1978; SB). In fact, the available literature for the nonrotating Görtler flow provides average values of the selected spanwise wave numbers that differ by up to a factor of 10. This fact indicates two things: the downstream vortex development is strongly influenced by the inlet flow and disturbance field (typical of a *convective* instability), and the wavelength selection mechanism is weak. The influence of system rotation on these two aspects of the Görtler instability has never been addressed before.

In a recent paper by Zebib and Bottaro (1993), from now on referred to as ZB, the nonlinear equations which describe the spatial development of Görtler vortices with system rotation were derived. A local linear stability analysis which included nonparallel effects on the growth of the boundary layer was also carried out. It was demonstrated that positive rotation (that is rotation in the sense of the basic flow) destabilizes the motion, while negative rotation stabilizes it. This influence of rotation has also been demonstrated by Aouidef *et al.* (1992). Curves of maximum growth rates in the wave-number–Görtler-number plane for different rotation numbers suggest that the preferred (linearly most amplified) dimensional spanwise wavelength of the vortices is larger for negative than for positive rotation. No experiments or nonlinear simulations of the rotating Görtler flow are available to support these statements. However, some experimental evidence exists for the rotating flat-plate boundary layer (Matsubara and Masuda, 1991) and for the rotating curved channel flow (Matsson and Alfredsson, 1990, 1994), which shows that positive rotation indeed enhances the growth of streamwise vortices, whereas negative rotation is stabilizing. An interesting observation made in both experiments was the increase in the number of vortices under the effect of positive rotation. In the flat-plate experiment by Matsubara and Masuda, the decrease of the average wavelength of the vortices with the increase of the angular speed of rotation is in agreement with arguments based on a local, parallel linear theory (see also Potter and Chawla, 1971). Matsson and Alfredsson (1994) found that when a specific wavelength was forced onto the flow by small roughness elements placed periodically along the span, a new vortex pair emerged between two existing pairs. They attributed this to an Eckhaus instability (Eckhaus, 1965), by which the flow would tend to adjust the imposed spanwise wavelength to a more favorable one (see also Bottaro, 1993; Guo and Finlay, 1994).

Some limited experimental results have been presented by Pexieder *et al.* (1993) for the rotating Görtler flow. Their flow visualizations indicated clearly that vortices start growing steadily within some range of rotation numbers, as was the case in SB for the case of no rotation. These initial experiments provide qualitative support to the stabilizing/destabilizing role of rotation.

Other studies related to the problem considered here are the stability of free shear flows subject to spanwise system rotation (Yanase *et al.*, 1993) and the effect of rotation on coherent structures in a turbulent

channel flow (Kristoffersen and Andersson, 1993). For this latter flow case, the pressure (suction) side of a channel receives an effect equivalent to that of positive (negative) system rotation in a boundary layer along a concave wall. Kristoffersen and Andersson (1993) report that with the increase of the rotation rate the number of vortex pairs close to the pressure side of the channel tends to increase. Conversely, the suction side is restabilized and might experience relaminarization for a sufficiently large rotation rate.

In this paper we perform numerical experiments by solving the steady, nonlinear equations of motion to assess the influence of rotation on the spatial development of the flow along a concave wall, and wavelength selection mechanism. These equations are parabolic, and are thus solved by straightforward marching, similar to that used by Lee and Liu (1992). In addition, the linearized version of these equations is also solved by a finite difference-spectral marching procedure, by which the amplification of vortices with a given spanwise wavelength is calculated. Linear and nonlinear results for different rotation numbers complement and confirm each other convincingly; both codes are then used to address issues of wavelength selection.

2. Mathematical Formulation

We consider the rotating boundary-layer flow over the concave wall with constant radius of curvature $\mathscr{R}$ subject to system rotation Ω with the axis of rotation coinciding with the axis of curvature (see Figure 1). Following ZB, we introduce the length scale ℓ, defined as the streamwise distance from the leading edge of the curved plate to the starting point of the calculation, and define the curvature parameter γ, the Reynolds number Re, and the Görtler number G by

$$\gamma = \ell \mathscr{R}^{-1}, \qquad Re = \frac{U_\infty \ell}{\nu}, \qquad G^2 = \gamma Re^{1/2}, \tag{1}$$

where U_∞ is the free stream velocity (assumed to be constant along x) and ν is the kinematic viscosity. The theory is developed for $\gamma \to 0$, $Re \to \infty$ such that $G = O(1)$, and the rotation number $Ro = \Omega \mathscr{R}/U_\infty$ is also $O(1)$. In a cylindrical coordinate system (r, θ, ζ) with corresponding velocity components (v_r, v_θ, v_ζ) we introduce the dimensionless boundary layer coordinates x, y, z:

$$x = \frac{\theta}{\gamma}, \qquad y = -\frac{(r - \mathscr{R})}{\ell} Re^{1/2}, \qquad z = \frac{\zeta}{\ell} Re^{1/2}, \tag{2}$$

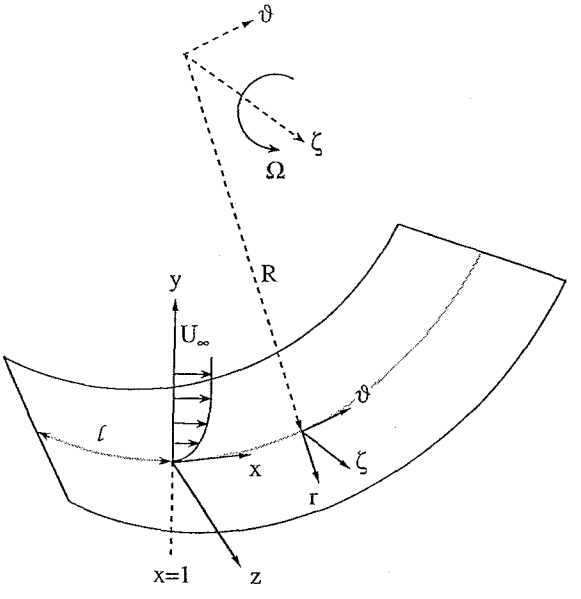

Figure 1. Sketch of the problem.

and the dimensionless velocities u, v, w, together with the pressure p:

$$u = \frac{v_\theta}{U_\infty}, \qquad v = -\frac{v_r}{U_\infty} Re^{1/2}, \qquad w = \frac{v_\zeta}{U_\infty} Re^{1/2}, \qquad p = \frac{p'}{\rho U_\infty^2} Re, \tag{3}$$

where ρ is the constant density and p' is the dimensional pressure. When these variables are substituted into the Navier–Stokes equations, expressed in cylindrical coordinates in the rotating frame of reference of Figure 1, the leading-order system is found to be

$$\frac{\partial u}{\partial x} + \frac{\partial v}{\partial y} + \frac{\partial w}{\partial z} = 0, \tag{4}$$

$$\left[u\frac{\partial}{\partial x} + v\frac{\partial}{\partial y} + w\frac{\partial}{\partial z} \right] u = \frac{\partial^2 u}{\partial y^2} + \frac{\partial^2 u}{\partial z^2}, \tag{5}$$

$$\left[u\frac{\partial}{\partial x} + v\frac{\partial}{\partial y} + w\frac{\partial}{\partial z} \right] v + G^2 u^2 = -\frac{\partial p}{\partial y} + \frac{\partial^2 v}{\partial y^2} + \frac{\partial^2 v}{\partial z^2} - 2RoG^2 u, \tag{6}$$

$$\left[u\frac{\partial}{\partial x} + v\frac{\partial}{\partial y} + w\frac{\partial}{\partial z} \right] w = -\frac{\partial p}{\partial z} + \frac{\partial^2 w}{\partial y^2} + \frac{\partial^2 w}{\partial z^2}. \tag{7}$$

The boundary conditions associated with the parabolic system (4)–(7) are taken to be

$$u = v = w = 0 \qquad \text{at} \quad y = 0, \tag{8a}$$

$$u_y = v_y = w_y = 0 \qquad \text{as} \quad y \to \infty, \tag{8b}$$

where the infinite field was truncated at $y_e = 50$. It was also checked that the adoption of conditions at y_e such as in Lee and Liu (1992),

$$u = 1, \qquad v_y = 0, \qquad w = 0,$$

produced the same results as the boundary conditions (8b). Most computations are performed for half a wavelength (π/α, where α is the wave number at $x = 1$), and along z the symmetry conditions

$$u_z = v_z = w = 0 \qquad \text{for} \quad z = 0, \frac{\pi}{\alpha}, \tag{8c}$$

are adopted. The numerical solutions of the nonlinear parabolic system is accomplished by the finite volume procedure described in Patankar and Spalding (1972). Briefly, the y–z computational domain is divided into rectangular cells with the grid points located at the geometric centers of these small cells. Additional boundary points are included to incorporate the boundary conditions. The discretized equations are obtained by integrating the conservation equations over control volumes having these cells as a base and extending a distance Δx in the streamwise direction. Local linear y and z dependence in any of the primitive variables is assumed, resulting in a second-order accurate scheme. Staggered location for the y–z velocity components is adopted to avoid unrealistic pressure fields and associated numerical instabilities. Streamwise marching is accomplished through a fully implicit first-order forward Euler scheme. For the parameter values of this work, we have determined that a 71×25 y–z grid (stretched in y and uniform in z) and $\Delta x = 0.02$ are adequate for computations covering half a wavelength. Numerous computations were also performed on a finer grid (121×50 and $\Delta x = 0.01$); each one of these latter calculations required of the order of 15 CPU hours on the Cray-2 supercomputer at EPFL.

2.1. Linear Stability Equations

We consider the spatial development of a perturbed Blasius profile:

$$\mathbf{u} = (U(x, y) + u_1(x, y, z),\ V(x, y) + v_1(x, y, z),\ w_1(x, y, z)), \tag{9}$$

where (U, V) is the Blasius solution to Prandtl's boundary-layer equations, which remain unchanged in the limit $y \to 0$. The linear stability equations are obtained by linearizing (4)–(7), and then reducing the system to a two-equation set in which the pressure and the spanwise disturbance velocity component are eliminated.

The resulting equations for the perturbation velocities u_1 and v_1 are

$$-\nabla^2 u_1 + U\frac{\partial u_1}{\partial x} + V\frac{\partial u_1}{\partial y} - V_y u_1 + U_y v_1 = 0, \tag{10}$$

$$-\nabla^4 v_1 + U\nabla^2\frac{\partial v_1}{\partial x} + V\nabla^2\frac{\partial v_1}{\partial y} + V_y\nabla^2 v_1 + V_{yy}\frac{\partial v_1}{\partial y} + V_{yyy}v_1 - U_{yy}\frac{\partial v_1}{\partial x} + 2V_y\frac{\partial^2 u_1}{\partial x\partial y}$$
$$+ 2V_{yy}\frac{\partial u_1}{\partial x} + V_x\left(\frac{\partial^2 u_1}{\partial z^2} - \frac{\partial^2 u_1}{\partial y^2}\right) + V_{xyy}u_1 + 2G^2(U + Ro)\frac{\partial^2 u_1}{\partial z^2} = 0, \tag{11}$$

with $\nabla^2 = \partial^2/\partial y^2 + \partial^2/\partial z^2$ and $\nabla^4 = \partial^4/\partial y^4 + 2(\partial^4/\partial y^2\,\partial z^2) + \partial^4/\partial z^4$. These equations are equivalent to those given by Hall (1983), with the addition of the rotation term; they are solved by downstream marching with an approach analogous to the one described by Bertolotti (1991), (see also Bertolotti *et al.*, 1992) for the solution of the so-called Parabolized Stability Equations, PSE. We consider disturbances $f_1 = (v_1, u_1)^T$, with the decomposition

$$f_1(x, y, z) = \tilde{f}(x, y)\exp\left(\int \sigma(x)\,dx + i\alpha z\right), \tag{12}$$

where $\tilde{f}(x, y) = [\tilde{v}(x, y), \tilde{u}(x, y)]^T$ is the mode shape of the perturbation. When substituting (12) into (10)–(11), the following parabolic equation results:

$$L\tilde{f} + M\frac{\partial \tilde{f}}{\partial x} = 0, \tag{13}$$

where L and M are 2×2 matrix operators in y given in the Appendix. The boundary conditions are taken to be

$$\tilde{u} = \tilde{v} = \tilde{v}_y = 0 \qquad \text{at} \quad y = 0 \text{ and } y_e, \tag{14}$$

and the initial conditions are taken from the local nonparallel stability problem (ZB). At each x-step, the energy growth is transferred to the exponential term, and this step is iterated until $\tilde{f}$ fulfills the normalization condition

$$\frac{\partial N}{\partial x} = 0. \tag{15}$$

Among the different choices of N (Bertolotti, 1991), we have taken $N = \int_0^{y_e} u_1^2\,dy$ which is a measure of the energy of the perturbation integrated over y. An initial function $\tilde{f}_0$ must be provided to initiate the downstream marching at $x = 1$, however, no initial value of σ is needed, since no x-derivatives of σ appear in the equations.

A local, nonparallel linear stability eigenvalue problem can be derived by setting M identically equal to zero. It should be noted that such local equations would be slightly different from those of ZB because of the inverted order of normal mode substitution and differentiation with respect to x. The results obtained with the two sets of local linear equations are indistinguishable from one another (Klingmann, 1993).

Equation (13) is solved by a second-order accurate finite-difference scheme in x and Chebyshev collocation (using from 50 to 80 points) in y, after mapping the infinite field in y to $(-1, 1]$ through the exponential mapping $y_t = 1 - 2\exp(-y/y_0)$, where y_0 is a value between 15 and 50. Extensive tests have been performed to validate the code and to select accurate, cost efficient, grids, both for the Orr–Sommerfeld and the Görtler problems (Klingmann, 1993).

3. Linear and Nonlinear Development of the Vortices

It has been shown experimentally (SB, among others) that the initial spatial development of Görtler vortices is steady. This is also true in the case of weak co- or counter-rotation of the system (Pexieder *et al.*, 1993). The development depends on a large number of variables, such as the shape and the streamewise position (ℓ) of the initial disturbances. Other parameters at play fix the values of Re, G, and Ro. Whereas the locally

scaled wave number α increases as $x^{1/2}$ and the local G as $x^{3/4}$ (Hall, 1983), the dimensionless wavelength parameter Λ, defined as

$$\Lambda = \frac{U_\infty \lambda'}{\nu}\sqrt{\frac{\lambda'}{R}} = G\left(\frac{2\pi}{\alpha}\right)^{1.5}, \tag{16}$$

remains constant at all streamewise locations (unless merging and/or splitting of vortices takes place and the physical wavelength λ' of the vortices is modified; this is discussed in further detail in Section 4). In this section we consider the influence of rotation and wave number on the downstream development of the vortices, and compare results obtained by linear and nonlinear analyses.

3.1. Influence of Rotation

Here we consider the influence rotation would have on previously reported experiments and computations (SB; Lee and Liu, 1992). The detailed measurements by SB were made at $U_\infty = 500\,\text{cm/s}$, $R = 320\,\text{cm}$, $\nu = 0.15\,\text{cm}^2/\text{s}$, for a vortex pair with a wavelength λ' of 1.8 cm, giving $\Lambda = 450$ (note that the average wavelength over the span was reported to be 2.3 cm, which corresponds to $\Lambda = 650$). The simulations are started at $\ell = 40\,\text{cm}$, so that at $x = 1$, $G = 6.756$, $\alpha = 0.3824$, and, as in Lee and Liu (1992), an initial disturbance (u_1, v_1, w_1) composed of the local linear eigenfunctions for $Ro = 0$[4] with $u_{1_{\max}} = 0.042$ is used to correspond to the experimental data in SB.

Figure 2 illustrates the "mushroom" growth corresponding to Ro between -0.2 and 0.2. Here contour plots of constant u are shown at five axial locations. The results obtained at $Ro = 0$ are in excellent agreement with previously published results (Lee and Liu, 1992). The stabilizing (destabilizing) influence of negative (positive) rotation which is predicted by the local linear analysis in ZB is verified by the nonlinear calculations. The penetration of low momentum fluid into the free stream, indicated by the 0.9 u-level, is seen to increase (decrease) according to $Ro > 0\,(<0)$. Further evidence of this influence can be seen from the "peak" and "valley" wall shear stress variation with x in Figure 3. At the mushroom stem (peak) positive rotation first decreases the wall gradient, with a subsequent increase which is more rapid the larger the rotation number. In the valley the spatial development is also faster at large positive Ro, and the maximum value attained is higher. Far downstream, the shear stresses at the peak and valley locations reach almost constant values which depend weakly on Ro.

The growth of the perturbation energy with x as a function of Ro (all other parameters fixed as stated above) is compared in Figures 4(a) and (b) with linear results, local and marching, respectively. The nonlinear perturbation energy is defined as

$$E = \int_0^{\pi/\alpha}\int_0^{y_e} u_1^2\, dy\, dz, \tag{17}$$

and the curves of linear growth shown in Figure 4 are computed according to

$$E = E_0 \exp\left(2\int_1^x \sigma\, dx\right), \tag{18}$$

where E_0 is the kinetic energy of the perturbation at $x = 1$. It can be seen that the local linear results of ZB slightly overestimate the growth of the Görtler vortices, whereas the linear marching results shown in Figure 4(b) faithfully reproduce the nonlinearly computed growth rates until quite large values of E. Far downstream, nonlinear saturation leads to a departure from the linearly predicted energy growth. An interesting observation to be made from Figure 4 is that, despite the large influence of rotation on the initial development, the vortices have the same perturbation energy regardless of Ro, once the nonlinear saturation stage is reached.

[4] Since there is really no formal mathematical justification for using the *local* eigenfunctions as initial conditions for the *marching* analysis, we have decided to use the same initial conditions (the local eigenfunctions at $Ro = 0$) for all the calculations, thus limiting the number of variables. The results show that the perturbation energy starts growing immediately for all Ro's, without noticeable transients.

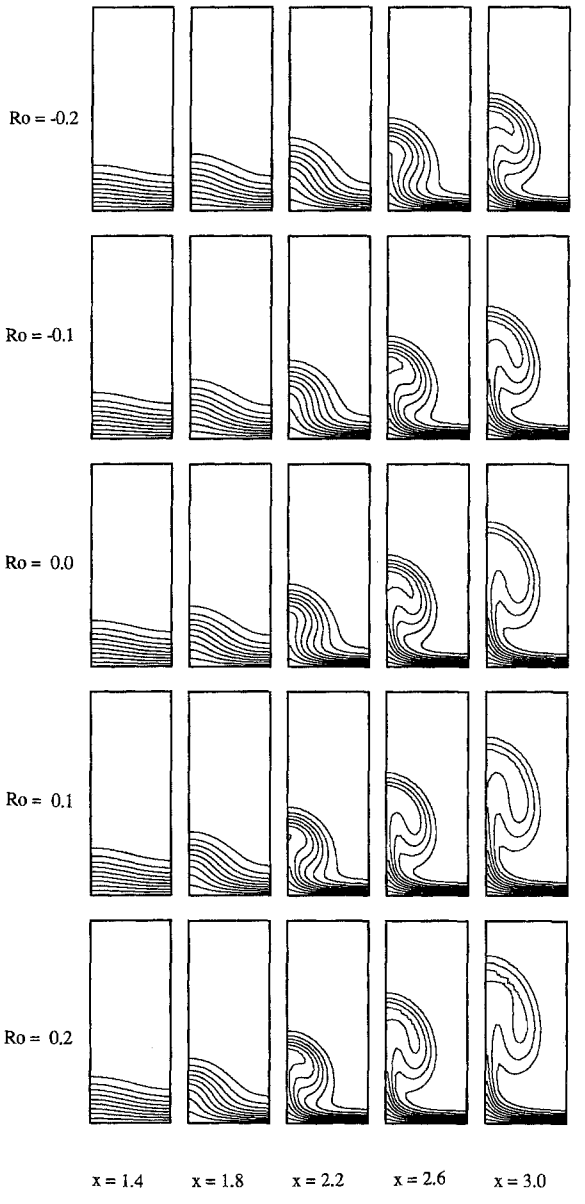

Figure 2. Development of vortices in x corresponding to different values of Ro and for a disturbance wave number $\alpha = 0.3824$. At $x = 1$, $G = 6.756$ and a perturbation proportional to the local linear eigenfunction at $Ro = 0$ normalized according to $u_{1_{max}} = 0.042$ is assumed. Deeper penetration of low momentum fluid into the free stream at larger values of Ro is observed. The y–z grid used is 121×50, with $\Delta x = 0.01$; the range of y in the plot is [0, 20] and the plots are scaled correctly. Spacing between neighboring isolines is 0.1.

3.2. Influence of the Initial Wavelength

To assess further the extent to which the linear marching theory is applicable, we have performed one more comparison between linear and nonlinear calculations at one Ro ($Ro = 0$, but it is safe to extrapolate qualitatively the conclusions to cases with $Ro \neq 0$) for two different wavelengths: $\Lambda = 75$ and 160. We fix ℓ at 10 cm (so that the initial $G = 2.39$), and the initial condition is taken as the solution to the local linear stability problem. In the nonlinear calculations the initial amplitude was taken to be $u_{1_{max}} = 0.05$. Figure 5(a) compares the linear and nonlinear energy growth for $\Lambda = 75$ and 160 in the absence of rotation. Note that the ratio of the specific energy levels (E/Λ) at saturation is about 2.7; the ratio of the absolute energy levels at saturation, $(E)_{\Lambda=160}/(E)_{\Lambda=75}$ is even larger and stands at approximately 4.5. Calculations performed for a range of wavelengths (not shown) indicate that saturation energies increase with Λ, but for each Λ there is no Ro-dependence. The fact that the larger vortices are more "vigorous" could also be deduced from Figure 5(b), where it is shown how the wall shear stress produced by vortices with $\Lambda = 75$ is consistently inferior to that induced by vortices with $\Lambda = 160$. Figures 6(a) and (b) show the nonlinear perturbation flow

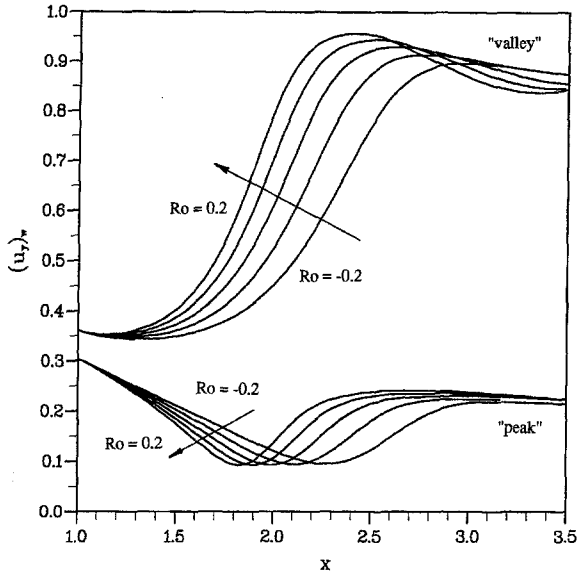

Figure 3. Variation of wall shear stress with x for the same conditions as Figure 1. The destabilizing influence of rotation can be inferred from the decrease (increase) in shear stress at peak (valley) locations.

fields for the two respective wavelengths at $x = 1.8$, 3, and 4.2 (the latter corresponding to $G \approx 7$). The energy grows faster for the higher wavelength, and, at $x = 4.2$, the maximum amplitude in u is 0.18 for $\Lambda = 75$ and 0.3 for $\Lambda = 160$. Despite such high amplitudes, the energy growth (Figure 5(a)) calculated with the nonlinear and linear codes are in good agreement up to and beyond $x = 4$.[5] The spanwise asymmetry and the formation of shear layers inclined with respect to the y-axis, visible at $x = 4.2$ in Figures 6(a) and (b), is also indicative of nonlinear effects (the linear theory is based on the assumption that the spanwise variation

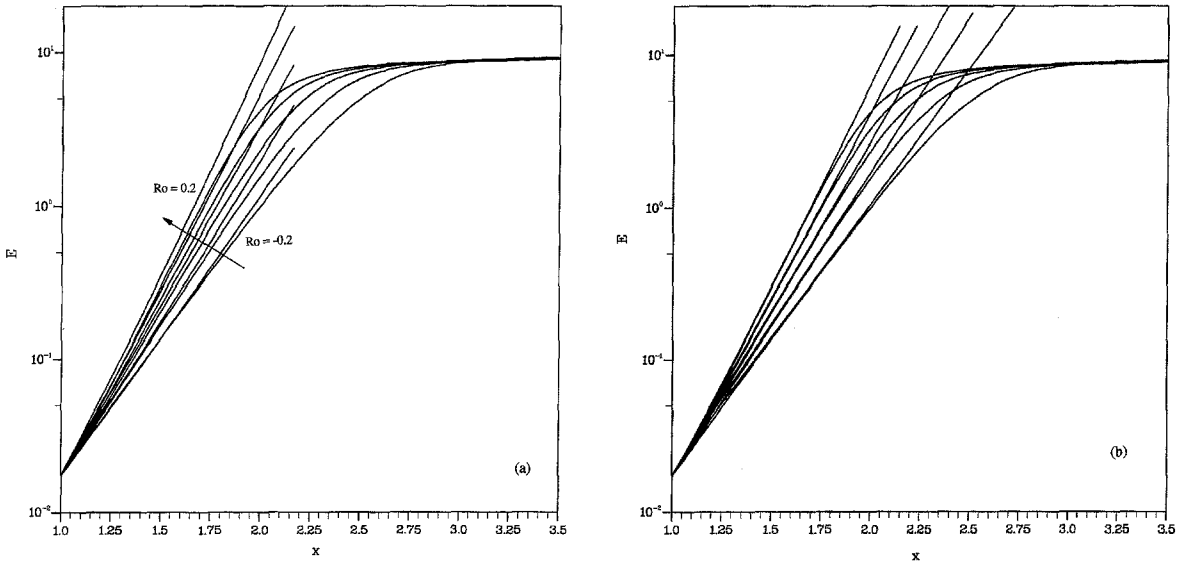

Figure 4. Growth of the perturbation kinetic energy E as defined in (17) and (18) corresponding to nonlinear and linear predictions, respectively. (a) Local theory and (b) marching theory.

[5] A slight "disagreement" between linear and nonlinear results is present at low x. It is due to the imperfect satisfaction of conservation balances in the nonlinear equations close to the starting point ($x = 1$). A nonlinear calculation which was carried out with $\Delta x = 0.01$ and with up to 10,000 iterations at each x step (for $1 \leq x \leq 2.5$) showed a perfect agreement with the linear marching results. It was deemed unnecessary to pursue such an expensive calculation.

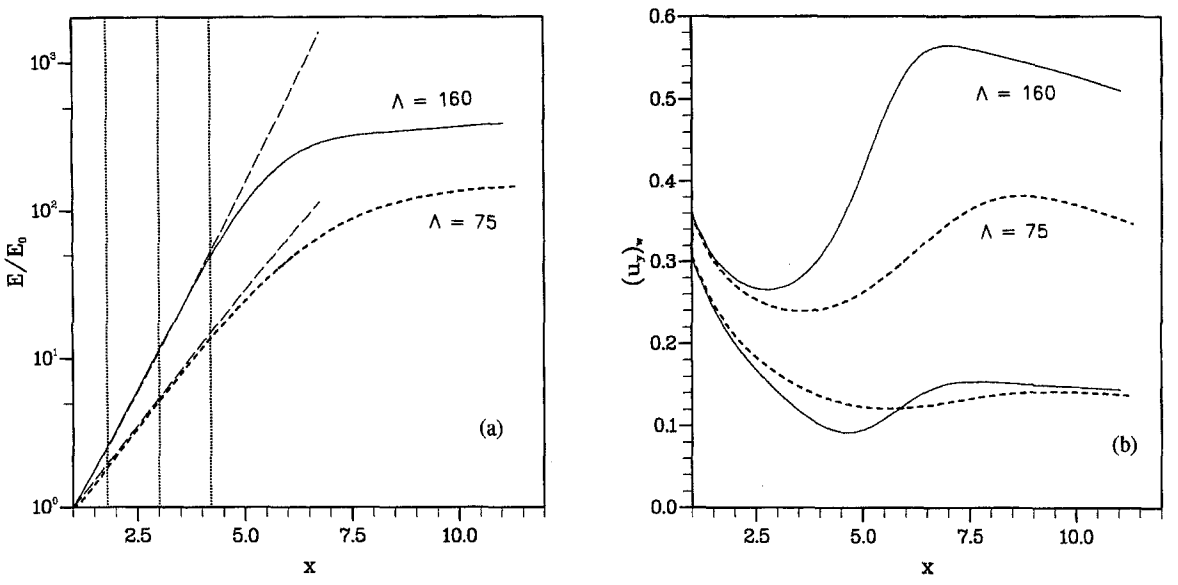

Figure 5. (a) Perturbation energy growth for $\Lambda = 75$ and 160. The long-dashed lines represent the linear marching results. (b) Wall shear stress at peak and valley regions for $\Lambda = 75$ and 160.

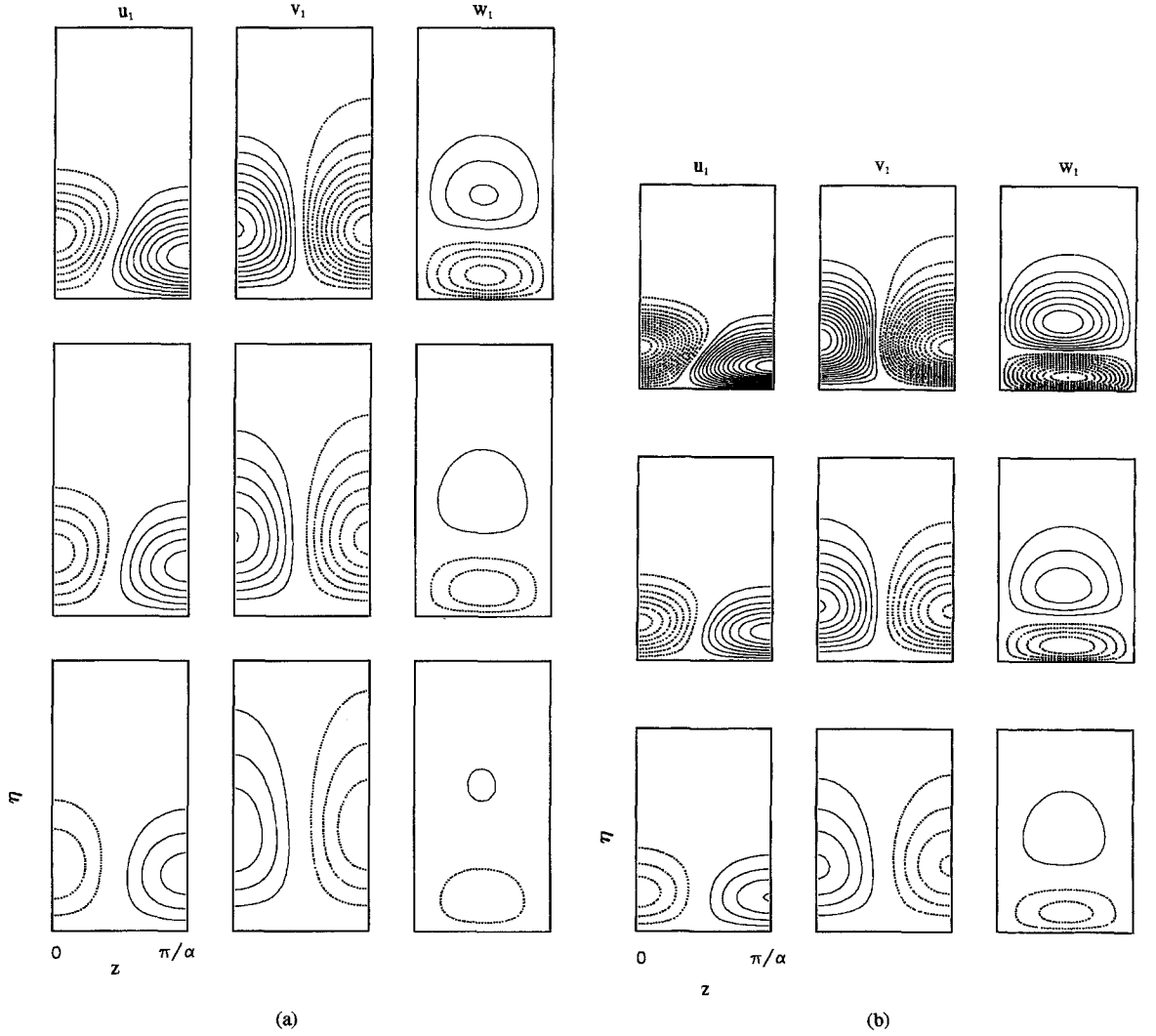

Figure 6. Deviation of the velocity field from the Blasius flow at three different downstream stations, from the bottom $x = 1.8$, 3, and 4.2. The spacing on the u_1 isolines is 0.02, and on v_1 and w_1 the spacing is 0.1. Positive values are shown with continuous lines, negative with dotted lines. (a) $\Lambda = 75$ and (b) $\Lambda = 160$.

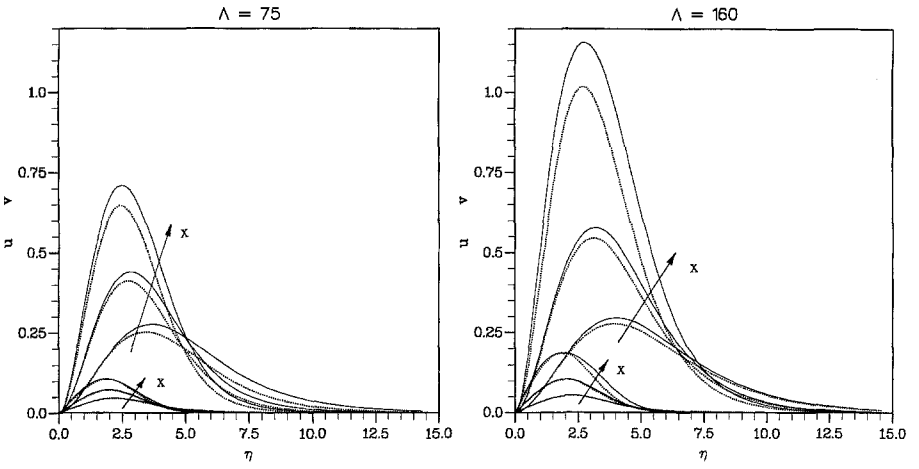

Figure 7. Comparison between linear and nonlinear mode shapes at the same three values of x as in Figure 6. The nonlinear results for u_{rms} and v_{rms} are shown with continuous lines and the linear results for u_1 and v_1 are dotted. The lower set of curves represent the streamwise components of the disturbance velocity at three x's and the upper set represent the normal components.

remains strictly sinusoidal). The spanwise-averaged longitudinal velocity is defined as

$$\bar{u} = \frac{\pi}{\alpha} \int_0^{\pi/\alpha} u \, dz, \tag{19}$$

and the spanwise r.m.s. of the u velocity field is defined as

$$u_{\text{rms}} = \left[\frac{\pi}{\alpha} \int_0^{\pi/\alpha} (u - \bar{u})^2 \, dz \right]^{1/2}. \tag{20}$$

Similarly, for v. The spanwise r.m.s. of the u- and v-fields of the nonlinear solution at three values of x are compared in Figure 7 with the mode shapes obtained from linear calculations. The comparison is made in such a way that the linear and nonlinear maximum values of u_1 and u_{rms} coincide, at each x. Once u_1 is defined, the variation of the vertical mode shape v_1 with η follows (η is the wall-normal similarity axis in the Blasius boundary layer). It can be seen that the relative size of v_1/u_1 of the linear solutions is slightly underestimated, however, the general agreement is remarkably good, even at $x = 4.2$.

In summary, both the z-averaged shape and the energy growth rate of Görtler vortices are well approximated by the linear theory even at u-amplitudes as high as 30% of the free-stream velocity (which correspond to energy amplification by a factor of 50, see Figure 5). Nonlinear effects result in an enhancement of the internal shear layers, which are important for the development of secondary instabilities and transition to turbulence (Bottaro and Klingmann, 1996). Such phenomena, which may already be operational before the stage of nonlinear saturation (SB), clearly cannot be reproduced by our steady calculations.

4. Wavelength Selection

The good agreement between linear and nonlinear results concerning the initial development of Görtler vortices indicates that the wavelength selection mechanism should be linear, insofar as it is the amplification rate which determines the dominant vortex wavelength. As will be seen in the following, there are also other aspects which play an equally important role, one being the upstream flow conditions, another being the nonlinear modification of the wavelength through an Eckhaus instability.

In the absence of rotation, theoretical considerations based on the optimal growth rates (see Floryan and Saric, 1984; Guo and Finlay, 1994) indicate a preference for vortices with a dimensionless wavelength parameter $\Lambda \approx 200$. This wavelength has also been found to dominate in experiments where disturbances were introduced uniformly over the span. In the experiments of Bippes and Görtler (1972), an isotropic field

of disturbances, induced by screens, was introduced into the incoming flow, and the average wavelength observed downstream was $\Lambda \approx 200$. This was confirmed later by Swearingen and Blackwelder (1986), who also studied the effect of various screen configurations on the wavelength selection. Hence, there is experimental evidence for the selection of vortices with the linearly most amplified wavelength, if the background disturbances are sufficiently broadband. However, larger wave numbers are usually found in experiments with low levels of free-stream turbulence, where disturbances are not triggered in a uniform manner (such as by a grid); e.g., SB observed an average spanwise wavelength of $\Lambda = 650$, and Tani (1962) found wave numbers of up to $\Lambda = 1900$. In these cases, small irregularities on the surface of the curved plate or in the free stream beyond experimental control are probably responsible for the wavelength selection.

4.1. Predictions from Linear Theory

According to the local linear theory given by ZB, the most amplified wavelength Λ lies in the neighborhood of 260 (160) for $Ro = -0.3$ (0.3). This can be inferred from Figure 7 of ZB by plotting lines at constant Λ and finding the wavelength which most closely coincides with the curve of maximum amplification. In the parametric study described below, the linear marching code was used to obtain solutions for a large number of Λ's and Ro's. Each run was initiated at $G = 1$ with the solution of the local stability problem. It was noted that varying the starting point of the downstream marching did not significantly affect the results; this is clearly a consequence of the fact that, in some asymptotic sense (Day *et al.*, 1990), the marching results tend toward the local results (which are independent of initial conditions and starting point) some distance downstream of the leading edge of the plate.

Figure 8 shows how the amplification rates vary with Λ and Ro, at fixed values of G. In all cases the dependence of σ on Λ (wavelength selection) is weak at low G where the linear amplification starts, giving similar amplification rates within a wide range of Λ's between 100 and 2000. As G increases, the region of intensively amplified Λ's becomes slightly narrower, particularly for positive Ro. Some nonlinear calculations did indeed show that vortices with widely varying Λ had practically equal amplification rates, and more so for $Ro < 0$ than for $Ro > 0$. With increasing Ro the most amplified wavelengths shift toward lower values. This is seen clearly in Figure 9, where the most unstable Λ (i.e., the Λ where σ is locally maximum at a given downstream position, G) is plotted as a function of Ro. When $Ro < 0$ the range of the most unstable Λ's varies quite broadly with G, whereas the variation is contained for $Ro > 0$ (Figure 9); for example, when $Ro = 0.5$, the most amplified Λ is in a narrow range centered on $\Lambda = 160$, whereas for $Ro = 0$, it varies between $\Lambda = 185$ and 240 as G increases from 2 to 15.[6] This fact could be interpreted as an indication that the wavelength selection mechanism is weaker at negative Ro, which is not surprising since the spatial development of the instability itself is weakened by counter-rotation. At low G and negative Ro, amplification rates are quite low, and the solutions are strongly dependent on the initial conditions. The results in this region should therefore be regarded with caution.

The interesting conclusion of the parametric study conducted here is that the selection mechanism for Λ is weak for all Ro, and particularly so at low G (or x), where the initial linear growth presumably starts. This fact underscores the strong sensitivity on initial conditions and the fact that a whole spectrum of initial perturbations may be amplified with practically equal growth rates. Receptivity is then likely to be a more important factor for the wavelength selection than maximal amplification rates.

Up to now we have considered vortices which already developed at the starting point of the calculation. Hence the whole initial receptivity phase, where perturbations organize themselves in a coherent form, is not represented. Linear results are often presented in the form of N factors, integrated from the point of neutral stability according to local linear theory. Such results may be misleading since in an experiment Görtler vortices do not necessarily start growing from the neutral point of the local analysis. As a matter of fact, the whole local linear stability problem is subject to justifiable criticism because it neglects the influence of initial conditions (Hall, 1983). Calculations using the present linear and nonlinear codes indicate that the initial development is very sensitive to the upstream condition used to initiate the marching, particularly at low G. This issue is addressed in more detail in the following subsection.

[6] If the accumulated energy growth (in the form of N factors) is considered instead of the local amplification rate σ, like in the analysis of Floryan and Saric (1984), the most amplified Λ's are slightly lower.

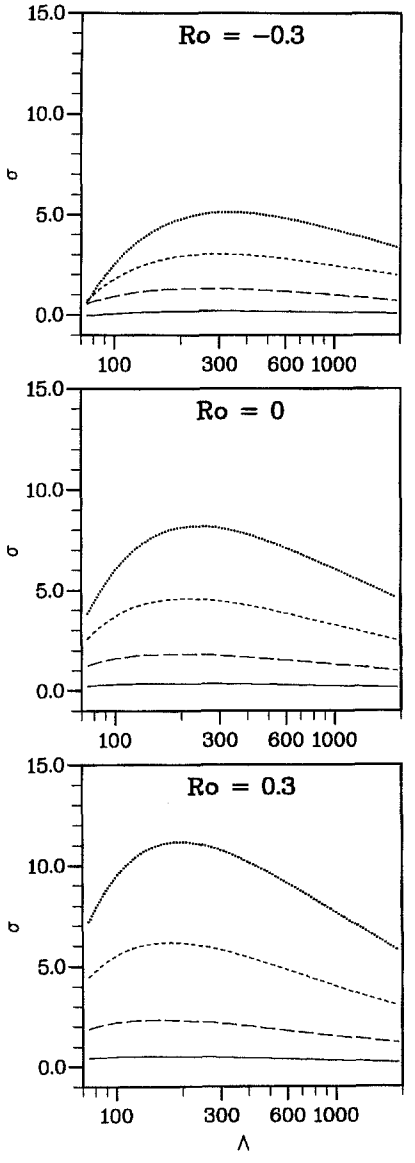

Figure 8. Amplification rates σ for different Λ at different constant values of G: ——, $G = 2$; — — —, $G = 5$; - - - - - -, $G = 10$; ·····, $G = 15$.

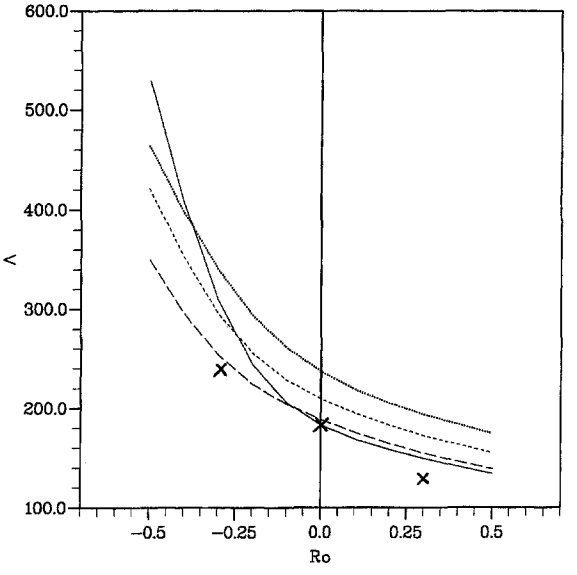

Figure 9. Variation of the most amplified wavelength with Ro, at different values of G: ——, $G = 2$; — — —, $G = 5$; - - - - - -, $G = 10$; ·····, $G = 15$. The crosses correspond to results of Section 4.2, for natural wavelength selection, when the vortices begin to appear.

4.2. Nonlinear Results for a Random Inlet Field

It is by now clear that a system subject to controlled perturbations can amplify vortices of almost any desired wavelength within a large range. On the other side, a randomly distributed field of incoming disturbances can be expected to develop into vortices with the linearly most amplified wavelength. This can be verified by considering a long (in z) test section and applying at the entrance of the computational domain a white-noise perturbation field. This is the strategy adopted in the nonlinear calculations of this and the following section. These runs start from $G = 6.756$ with a computational box of dimensionless spanwise length equal to 89.7. The inlet conditions used are stationary; this is an adequate representation of the situation in which vortices are triggered by upstream grids or wall roughness. On the other hand, an unsteady analysis should be employed when free-stream turbulence or acoustic disturbances are dominant.

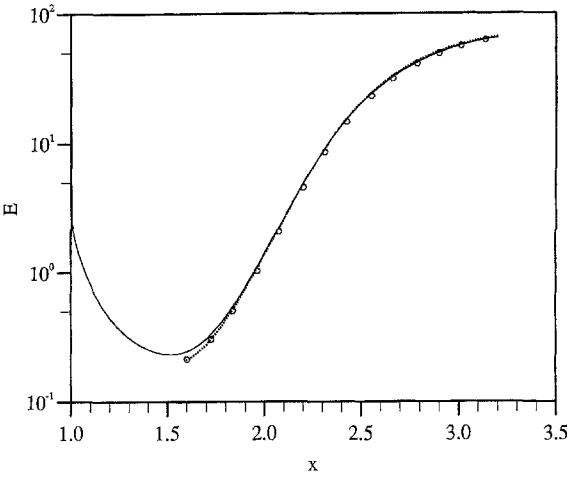

Figure 10. Mesh resolution study. ——, mesh: 71 × 151, $\Delta x = 0.02$; ·····, mesh: 57 × 121, $\Delta x = 0.025$; ○, mesh: 91 × 181, $\Delta x = 0.0125$.

In this latter case the vortices could present a continuous temporal evolution, with seemingly chaotic merging and splitting events. Clearly, these phenomena are excluded by our steady simulations.

4.2.1. *Mesh Resolution Requirements.* First we establish the grid-size distribution necessary to resolve adequately the vortical structures in the long cross section under consideration.

A perturbation field composed by random noise of amplitude varying between -0.042 and 0.042 in each of the three velocity components is applied at the inlet of our computational domain, for the case $Ro = 0.3$. The first grid employed has the same number and distribution of points along x and y as in the previously described calculations, namely 71 control volumes along y, and a streamwise marching step equal to $\Delta x = 0.02$. In the spanwise direction 151 control volumes are used. The curve of the computed perturbation energy (defined by (17)) versus x is displayed in Figure 10. An initial phase appears in which E decreases, signifying decay of many components of the initial conditions when projected on the eigenfunction space of the linear problem, followed by a phase, for $x \geq 1.52$, of growth and nonlinear saturation. Two other grids, one coarser and one finer, have been tested to validate the present run. Because of the completely uncorrelated nature of the disturbance flow field at $x = 1$, it turned out to be impossible to interpolate the velocity field there properly onto different grids to produce identical, or even similar, downstream evolutions. We have thus resorted to interpolating the velocity distribution at $x = 1.6$, close to the initial growth phase of the vortices, since at this point a more correlated distribution of perturbation variables has been produced by the application of the governing equations of motion. Even then, the initial point of vortex growth differs slightly among the three grids adopted.[7] The starting points of the two new grids have a slightly lower perturbation energy compared with the original run; the downstream developments, however, closely follow one another in the linear growth regime as well as in the nonlinear phase. Furthermore, the details of the disturbance fields are very well captured by all three simulations.

4.2.2. *Influence of Random Noise Distribution.* In this and all the following numerical simulations the mesh adopted is the "intermediate" one, whose adequacy has been established above. The two calculations described here start from the same global disturbance amplitude, but with different random noise distributions. Results for $Ro = 0.3$ are displayed in Figures 11 and 12. The perturbation energies differ between the two cases, except clearly for $x = 1$, and the saturation levels reached are also slightly different. The latter is an effect of the different filtering selection actuated by the equations in the linear regime when E decreases, and of the different average wavelengths achieved in the two cases in the nonlinear stages. Note, however, that the streamwise extent of the initial energy-decreasing phase is the same (from $x = 1$ to about $x = 1.5$) for the two different random noise distributions. The streamwise velocity fields are shown in Figure 12 at five different x values; the spatial evolutions produced are qualitatively similar. Most of the

[7] It is also to be noted that through bilinear interpolation we introduce approximations locally proportional to Δy and Δz.

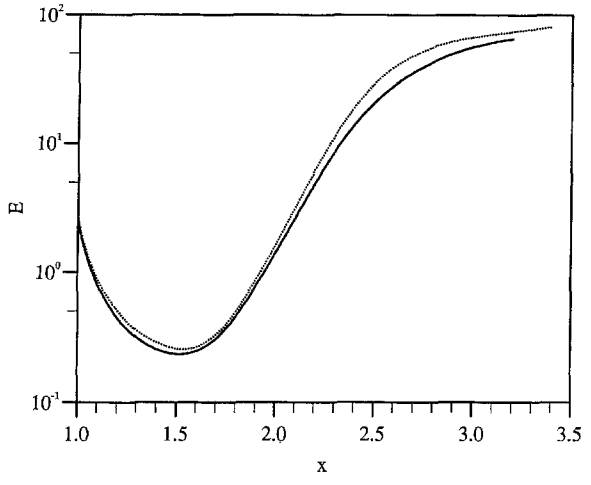

Figure 11. Perturbation energy versus x, for two different inlet noise distributions but same initial amplitude levels; $Ro = 0.3$.

vortices are bent toward a side highlighting the disparity in streamwise vorticity levels on either side of the vortex pair. Such asymmetries are due to interactions originating from an Eckhaus instability (Guo, 1992; Guo and Finlay, 1994).

The main difference between the two cases lies in the average wavelength produced; the flow field on the right-hand side of Figure 12 (corresponding to the dotted curve in Figure 11) presents consistently one less upwash region than the case on the left. Simple hand counting of the visible upflows in the cross sections indicates that there are 11, 10, and 9 pairs for x equal to, respectively, 2.4, 2.8, and 3.2 (flow field on the right). Even this count is approximated, since some vortices do not have a "companion" and resemble cross-flow vortices (see Malik *et al.*, 1994). Further discussions on the wavelength selection, together with an interpretation of the energy curves, are provided in the next two subsections.

4.2.3. *Effect of the Initial Amplitude Level.* Starting with the same white noise but with different amplitudes, the disturbance energy for $Ro = 0.3$ decreases (Figure 13(a)); this occurs over an extent which is *independent* of the initial amplitudes. The perturbation amplitudes chosen on the different velocity components are 1%, 4.2%, 10%, and 33.3%, corresponding to curves 1, 2, 3, and 4, respectively. Thus, the boundary-layer equations act as a linear filter between $x = 1$ and $x_0 = 1.52$ (dotted vertical line in the figure)

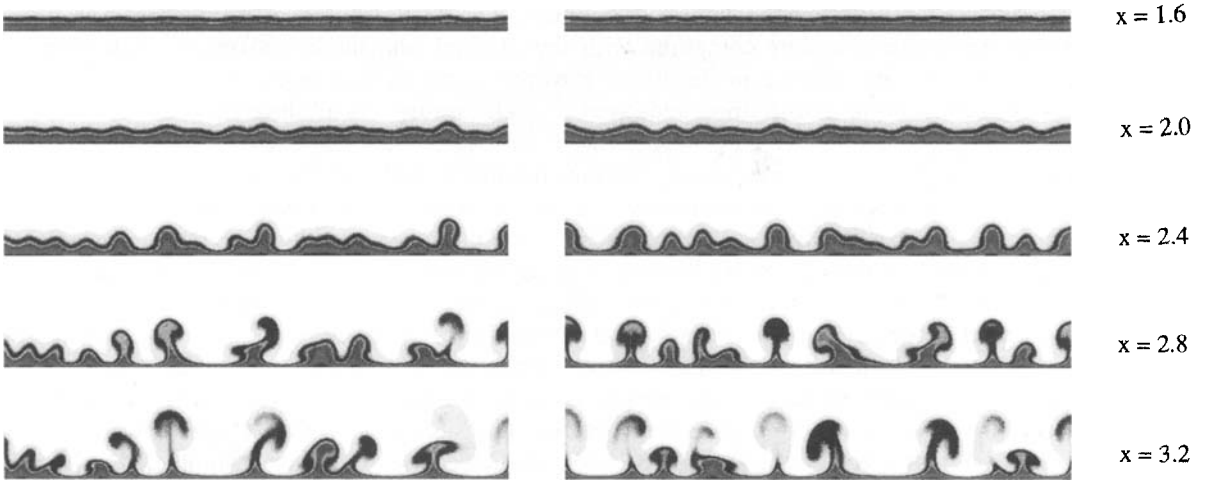

Figure 12. Contours of the streamwise velocity fields for the two cases of Figure 11. The plots are scaled correctly.

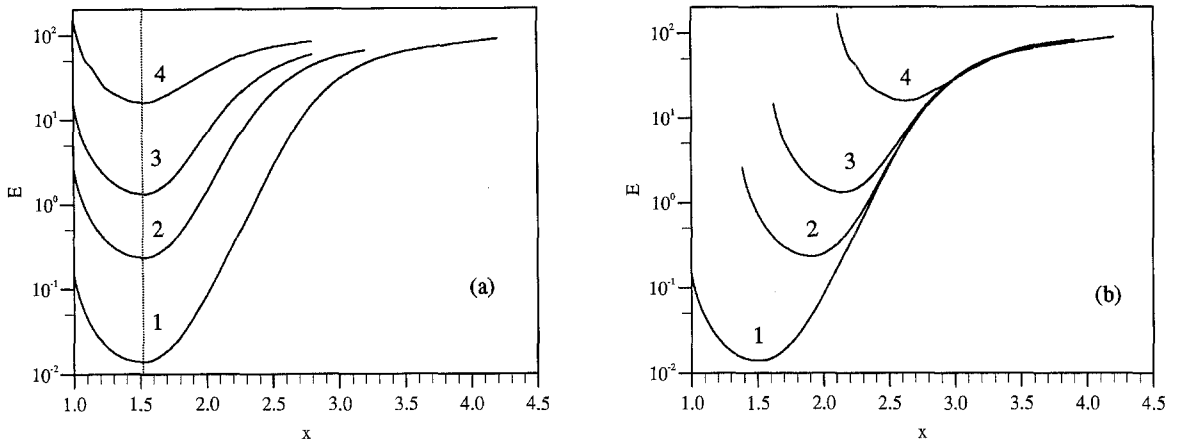

Figure 13. (a) Perturbation energy versus x, $Ro = 0.3$. Different initial amplitude levels. (b) Collapse of the curves when a "virtual origin" is introduced.

for whatever initial perturbation amplitude. Quasi-exponential growth follows x_0 according to

$$\frac{A}{A_{0_i}} \approx e^{2\sigma(x_i - x_0)}, \tag{21}$$

where A is the amplitude of the energy perturbation, σ is the linear growth rate, and $x_i > x_0$, $i = 1, 2, 3, 4$, is the streamwise location where the level A is achieved for any initial level A_{0_i}. Thus, we find, using the fact that $A_{01} = 0.014$, $A_{02} = 0.233$, $A_{03} = 1.329$, and $A_{04} = 16.130$ at the common minimum point of the three curves, $x_0 = 1.52$, the relations

$$\begin{aligned} x_1 - x_3 &\approx 1.61\,(x_1 - x_2), \\ x_1 - x_4 &\approx 2.50\,(x_1 - x_2). \end{aligned} \tag{22}$$

This scenario is confirmed by sliding curve 2 horizontally distance L until it coincides, for x large enough, with curve 1. When curve 3 is likewise shifted a distance $1.61L$ to the right and curve 4 a distance $2.5L$, we find the nice collapse indicated in Figure 13(b). The overlap of the four curves for some x range till nonlinear saturation is a powerful result which indicates conclusively that a linear receptivity operation is actuated by this flow when subject to steady, random perturbations. A similar conclusion was arrived at by Pexieder *et al.* (1993). They steadily triggered organized Görtler vortices through small amplitude jets, located near the leading edge of a curved test section. By simply using, as a measure of growth, the vertical size h of the mushroom structures visualized with dye, and through variation of the initial perturbation amplitude of the jets, they were able to find a similar collapse of h versus x by relative shifting of curves measured starting from different initial perturbation levels. This, in fact, is equivalent to finding some kind of *virtual origin*, from which point on common growth takes place. Fully grown vortices are shown in Figure 14 through isocontours of u_1 at $x = 3.2$ (for the flow situation corresponding to curve 1), $x = 2.8$ (case 2), $x = 2.6$ (case 3), and $x = 2.2$ (case 4). The similarities are evident, although there is not a perfect coincidence between the different cases because the four stations displayed are not exactly the "same." The value of L, defined above, is equal to about 0.4; $1.61L$ and $2.5L$ correspond to distances $x_1 - x_3 \approx 0.64$ and $x_1 - x_4 \approx 1.0$ (so that (22) is satisfied).

These results clearly demonstrate that the Görtler number, by itself, is not a sufficient measure to define the state of growth of a vortex pair. Some other quantity, as yet undefined, is necessary; such a quantity should take into account amplitude level and structure of the inlet perturbation field. It is, in fact, a receptivity parameter.

Finally, it is to be noted that the same qualitative behavior described in this and the preceding subsections is expected to occur at different values of Ro.

4.2.4. *Effect of Rotation on the "Natural" Wavelength Selection.* Starting from the same random noise distribution and level as case 1 above, three cases have been compared: $Ro = -0.3, 0$, and 0.3. In Figure 15

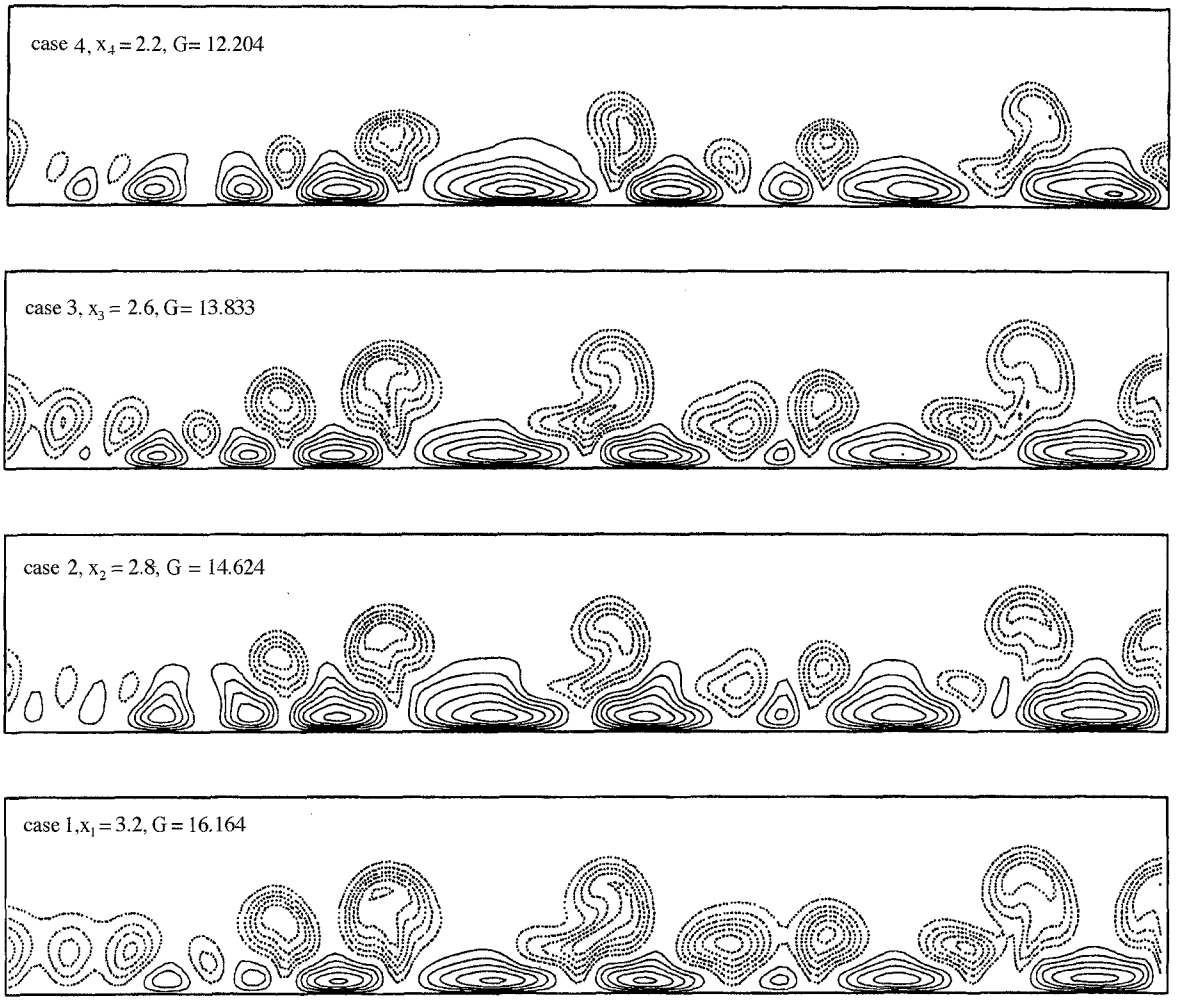

Figure 14. Streamwise perturbation fields for the four cases of Figure 13, at four different $x(G)$ values. The plots are scaled correctly in the y–z plane, and the vertical scale extends to $y = 15$. Positive values of u_1 are shown with full lines, negative values with broken lines, and the zero lines are omitted. The spacings between adjacent isolines is 0.1.

we have plotted isolines of the streamwise velocity for these three cases at different downstream positions x. As already shown, the vortices start growing at random locations in z, and vortices with different individual wavelengths and amplitudes coexist at each x. The average wavelength at the x-position where the vortices first appear can be obtained by simply counting the number of outflow regions; this gives $\Lambda = 125$ (for $Ro = 0.3$), 181 ($Ro = 0$), and 250 ($Ro = -0.3$). Because of the irregularity of the vortices, the value of the average wavelength is approximate to $\pm 10\%$. It is also clear (Figure 12) that different inlet noises would produce slightly different results. The average "natural" wavelengths obtained in this way are in agreement, although slightly lower, with those predicted by linear stability (see Figure 9). This confirms that, on the average, the linearly most amplified wavelength is selected when the flow is subjected to random inlet perturbations.

The distribution of the perturbation energy E with the downstream distance x is represented in Figure 16 for the three values of Ro shown by the thin solid lines. For each Ro, in correspondence to the point of steepest positive gradient of the solid thin lines E versus x, we have plotted the curves of linear growth (dotted lines) for the initial average values of Λ of 125, 181, and 250 (for $Ro = 0.3, 0$, and -0.3, respectively). Note that the nonlinear amplification rate (i.e., the slope of the full lines in Figure 16) is always lower than that of the linear solution for the average Λ before the two curves intersect. This could be ascribed to

a number of reasons, among which is the absence of a monochromatic wave and, hence, the coexistence of vortices at different growth stages in the nonlinear simulations. The bold line in Figure 16 is the difference between the full solution and the linear solution for the average Λ (valid up to the point of intersection between the linear and nonlinear curves). Interestingly, this line, indicative of the linear receptivity phase, is not a function of Ro. Although the representation chosen is not unique (different linear growth curves could be employed, for example) it is instructive to think of the initial phase of the vortices as the coexistence of two events: the damping of the disorganized noise and the creation of patches of organized vorticity near the solid wall (see also Figure 17). Hence, we can introduce three cross-over points x_i ($i = 1, 2, 3$ for, respectively, $Ro = 0.3, 0, -0.3$), defined as the points of intersection of the dotted lines and the bold solid line. These cross-over points are equal to 1.7, 1.9, and 2.2 for Ro of, respectively, 0.3, 0, and -0.3. For $x > x_i$, there is a clearly distinguishable linear amplification region, where the vortices appear and grow (see Figure 17).

A notable difference between the three cases computed is the fact that Λ changes significantly for the positive rotation case, in the range of x considered, because of the merging of vortices. For $Ro = 0.3$, there are 13 vortex pairs at $x = 2$ (average Λ is 125), 12 at $x = 2.4$ ($\Lambda = 138$), 11 at $x = 2.8$ ($\Lambda = 157$), and 10 at $x = 3.2$ ($\Lambda = 181$). To a lesser degree this also occurs for $Ro = 0$, where only one merging event occurs for $2.2 < x < 2.4$, whereas the average wavelength remains constant for the negative value of Ro. This points out the fact that the case $Ro = 0.3$ is more susceptible to an Eckhaus instability than $Ro = -0.3$; hence, in the nonlinear regime for $Ro > 0$ an Eckhaus criterion should be used to interpret the selected wavelength.

The vortex merging at positive Ro can be clearly observed both in the contours of u in Figure 15(c) and in the streamwise vorticity field of Figure 17. A clear example is the merging of two vortex pairs near the center of the cross section at $x = 2.4$ into one pair at $x = 2.8$; a similar phenomenon is also produced between $x = 2.8$ and 3.2. Both events are marked by vertical arrows in Figure 17 for easy identification. Typically, the merging involves two vortex pairs, where one pair is much stronger than its neighbor. The stronger pair "jumps" above the weaker one with a spanwise shift of half a wavelength. In so doing, at first one cell of the weaker pair is annihilated and secondly two corotating cells (orginally belonging to two different pairs), placed one above the other, merge into one. The end result is one strong pair (central pair at $x = 3.2$) with the upwash region somewhat inclined, and a tilting of the neighboring vortices. This process is likely to be the cause of the irregularity of vortices seen to prevail in many experimental flow visualizations. We now wish to present some parallels between longitudinal vortices and organized structures in wall-bounded flows. Although these comparisons are somewhat speculative, it appears that the Görtler flow represents a good "laboratory" on which to study the dynamics of wall vortices, with a view toward flow control.

4.2.5. *Similarities to Turbulent Coherent Structures.* The flow patterns computed present a clear resemblance to organized (coherent) structures of transitional and turbulent boundary layers (see Blackwelder, 1983). Robinson (1991) reports that the buffer-layer region is densely populated with relatively strong quasi-streamwise vortices which play a major role in the formation of low-speed streaks. To verify whether the similarities are more than just qualitative, the dimensions of the vortices are rescaled into wall units, using the viscous length characteristic of the diffusion of vorticity away from the wall. Such a length scale, commonly used in turbulent boundary layers, is, in dimensional form,

$$l^+ = \left[\frac{\nu}{\partial u/\partial y|_w} \right]^{0.5}. \tag{23}$$

By using the scaling of (2)–(3) it is easy to find

$$l^+ = \mathrm{Re}^{-0.25} \left. \frac{\partial u}{\partial y} \right|_w^{-0.5}, \tag{24}$$

where everything is now dimensionless as by (2). $\partial u/\partial y|_w$ is taken to be the average across the span at each given x-position (note that l^+ varies with x, since the wall shear stress changes with x, and so does the spanwise wavelength). The results obtained for the average spanwise wavelength of the vortices λ^+, and the average location of the cell centers y_c^+ (defined as the y location where the spanwise integral of w^2 has

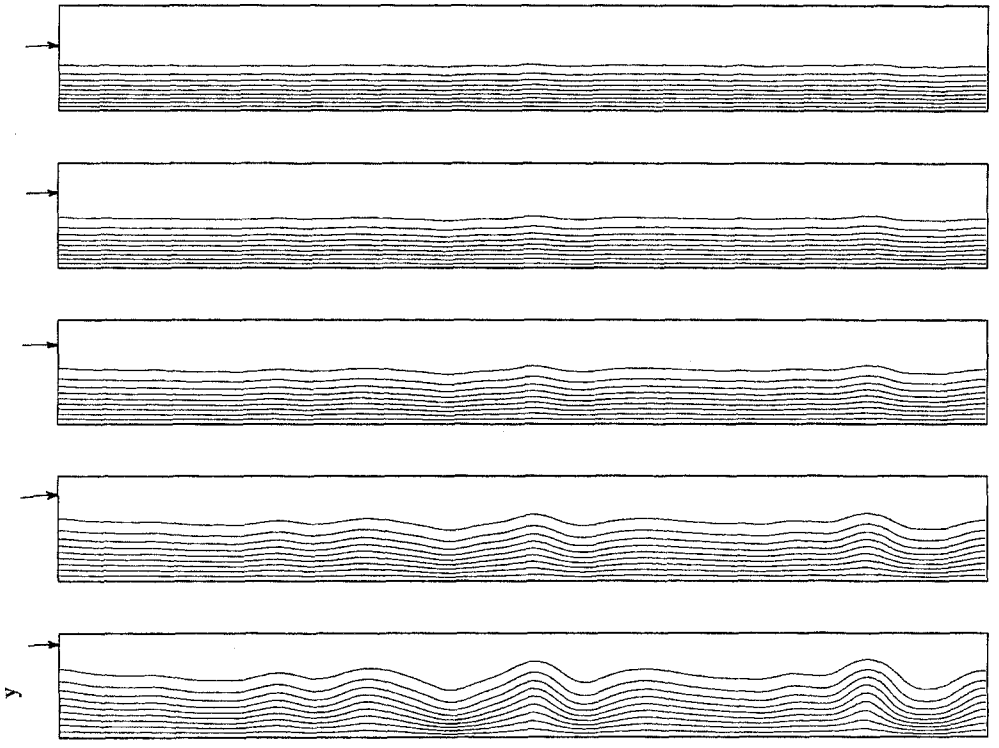

(a)

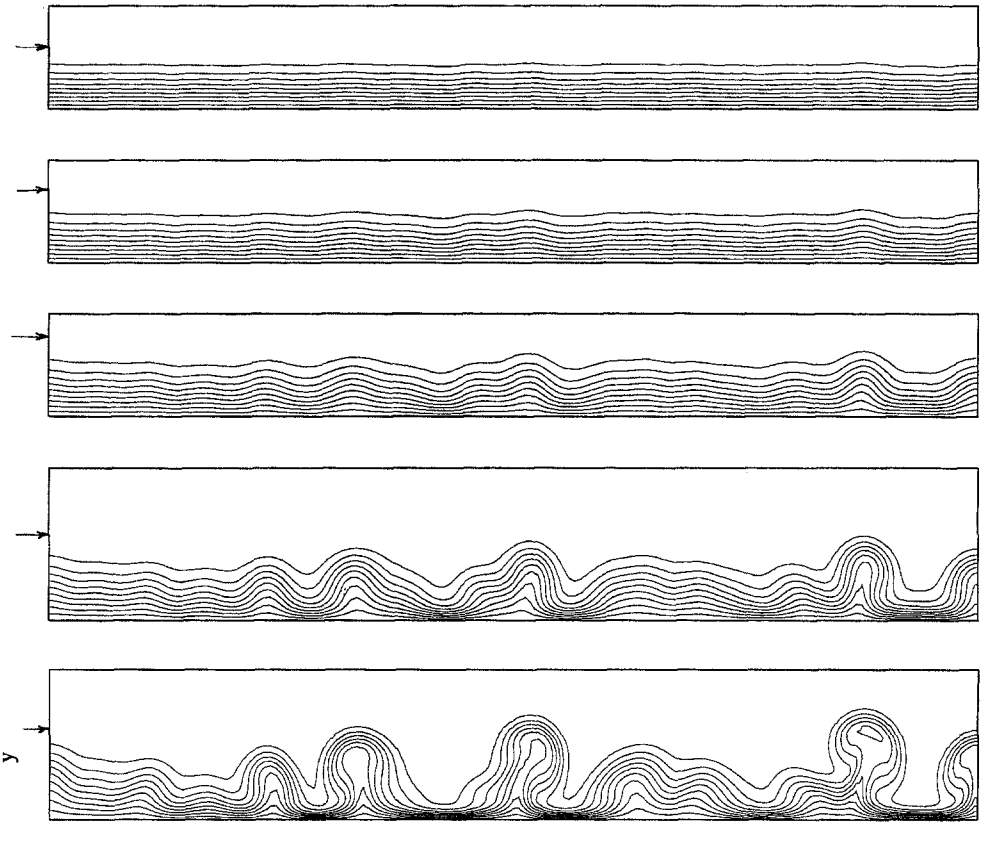

(b)

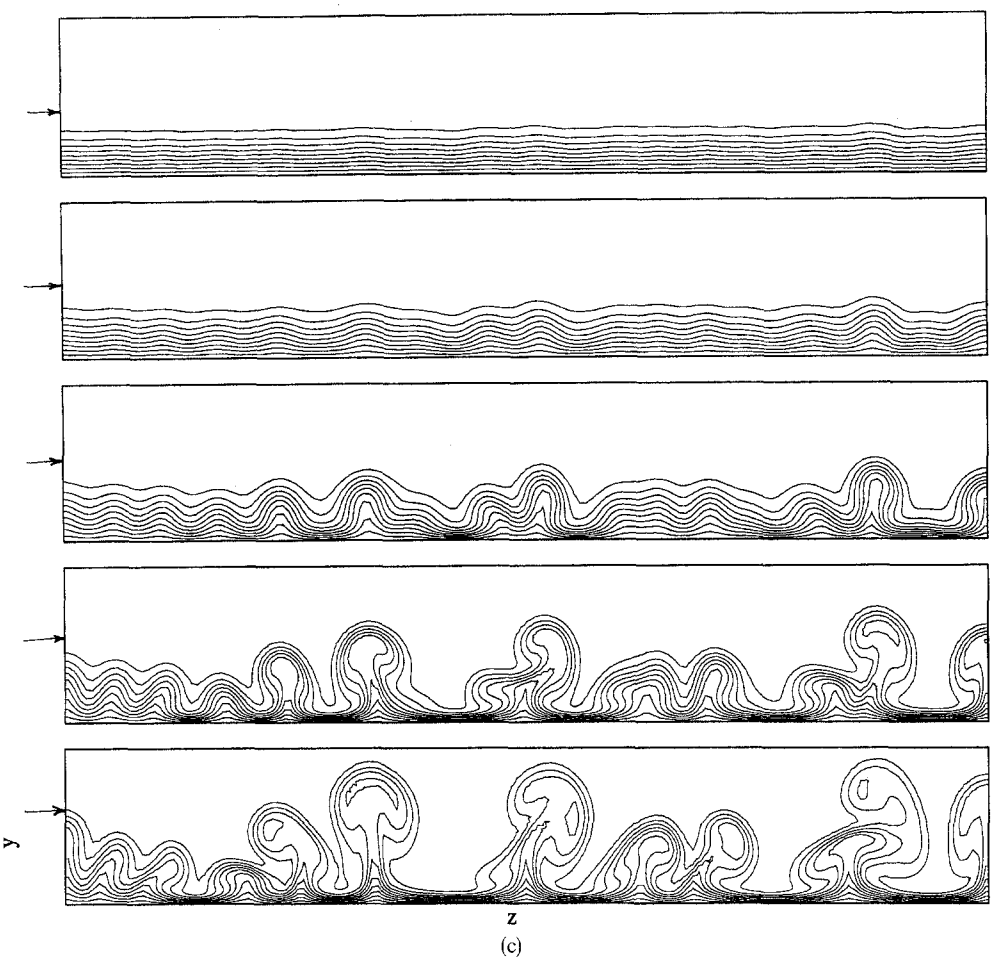

Figure 15. (a) Isolines of the streamwise velocity for $Ro = -0.3$ at, from the top, $x = 1.6, 2, 2.4, 2.8, 3.2$. The isolines are spaced 0.1 apart. Note that, for comparison purposes, a small horizontal arrow has been drawn in correspondence to the edge of the undisturbed Blasius boundary layer, i.e., $\eta = 5$, at each x station. (b) $Ro = 0$, same x values as (a). (c) $Ro = 0.3$, same x values as (a). A tendency toward further merging events, for $x > 3.2$, manifests itself.

a minimum) are summarized in Table 1. There we also report the average spanwise wavelength Λ and η_c, the cell centers in Blasius similarity coordinate, for the flow cases discussed in Section 4.2.4. Limited numerical experiments have shown that different inlet noise distributions yield spanwise wavelengths Λ and λ^+ differing from those quoted in Table 1 by at most 10% (see also Section 4.2.2); on the other hand, η_c and y_c^+ remain practically unchanged. Note that for $Ro = -0.3$, $x = 2$ (still below the cross-over point x_3), vortices are not yet identifiable.

These dimensions are in the range of those typically quoted for streamwise or quasi-streamwise vortices in the wall region of low Reynolds number turbulent boundary layers. The mean spacing between low-speed streaks in the sublayer is about 100 wall units, and the vortex centers are typically located at $y^+ < 50$. A note of caution is in order, however: In the definition of l^+ the Reynolds number appears. We have used the value of Re corresponding to the experiments of SB, but it should be clear that Re is not a parameter in (4)–(7), and that an infinite number of combinations of Re and γ (ratio between the distance from the leading edge ℓ and the radius of curvature $\mathscr{R}$) can produce the value of $G = \gamma^{0.5} Re^{0.25} = 6.756$ used in the simulations. We could, alternatively, write

$$l^+ = G^{-1} \gamma^{0.5} \left. \frac{\partial u}{\partial y} \right|_w^{-0.5}, \tag{23}$$

and a dependence on γ appears. Our results have been computed for $\gamma = 0.125$ taken from SB. If, for

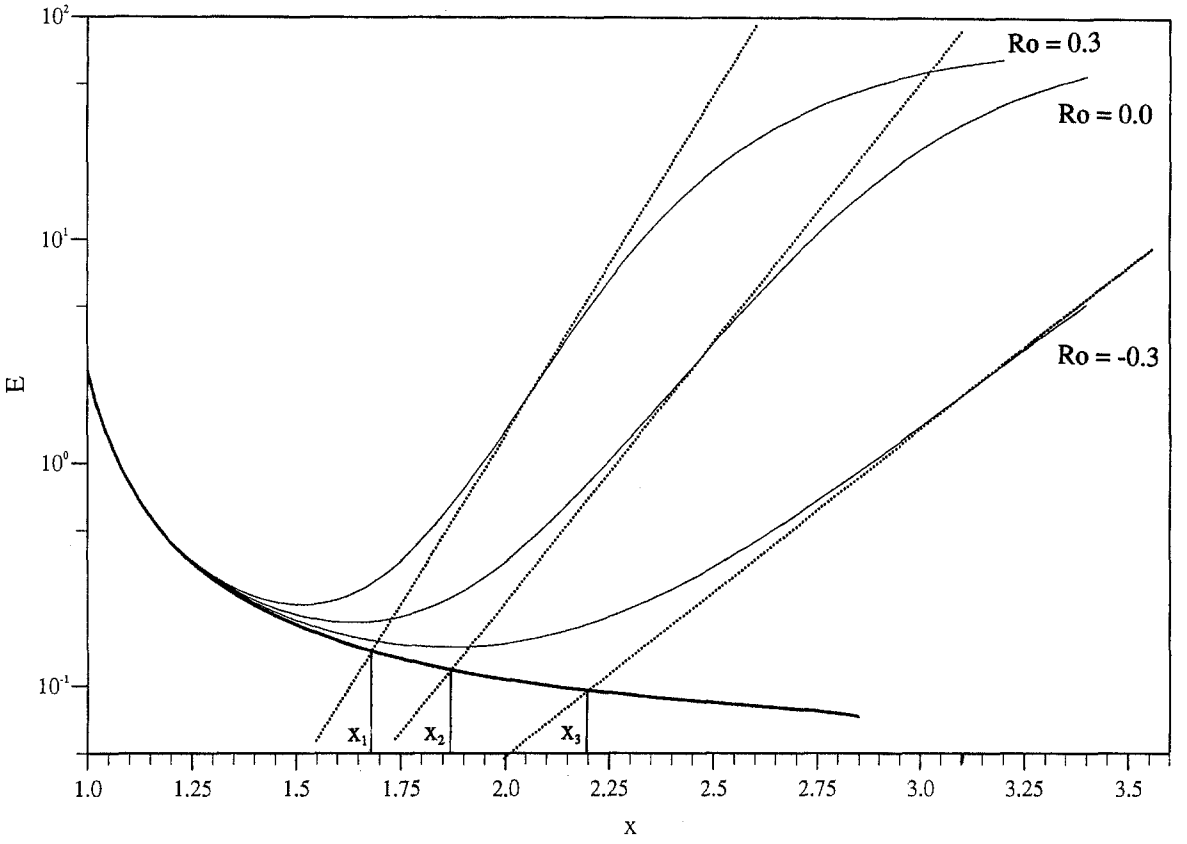

Figure 16. Spatial perturbation energy growth. The initial phase in which the random noise is damped is shown with a bold solid line, the linear growth curves corresponding to the average wave numbers computed at each *Ro* are shown with dotted lines, and the nonlinear simulation results (which for x sufficiently low are given by the linear superposition of the two previous curves) are represented with thin full lines.

example, $\mathscr{R}$ was twice as large or small (with ℓ and G fixed), the value of l^+ would differ by a factor of $\sqrt{2}$ (and all quantities scaled in viscous units would change accordingly).

The average spanwise wavelength scaled in wall units increases rapidly when the system is subjected to a positive rotation, whereas it remains practically constant for zero and negative system rotation. From inspection of the numbers presented in Table 1 we can also observe that as the vortices detach from the wall with the increase of x, their centers move upward both in physical units and in wall units. This is particularly clear for positive *Ro*, where merging events contribute to the ejection of vortices from the wall. This is in broad agreement with recent findings by Kristoffersen and Andersson (1993) concerning the effect of rotation on sublayer streaks in a turbulent boundary layer.

5. Concluding Remarks

In this paper results for nonlinear spatially developing Görtler vortices subject to system rotation have been presented. Comparisons with recent nonparallel linear theories, using both local and nonlocal solution procedures, have also been shown. Both approaches produce similar solutions to the linear problem; however, the nonlocal (marching) approach gives more accurate results, when compared with the fully nonlinear solutions. Extensive comparisons between linear and nonlinear marching results show good agreement until quite large amplitudes of perturbation, both for the z-averaged shape and the growth rate of the vortices. Given its speed of execution, the linear marching code promises to be a powerful tool for

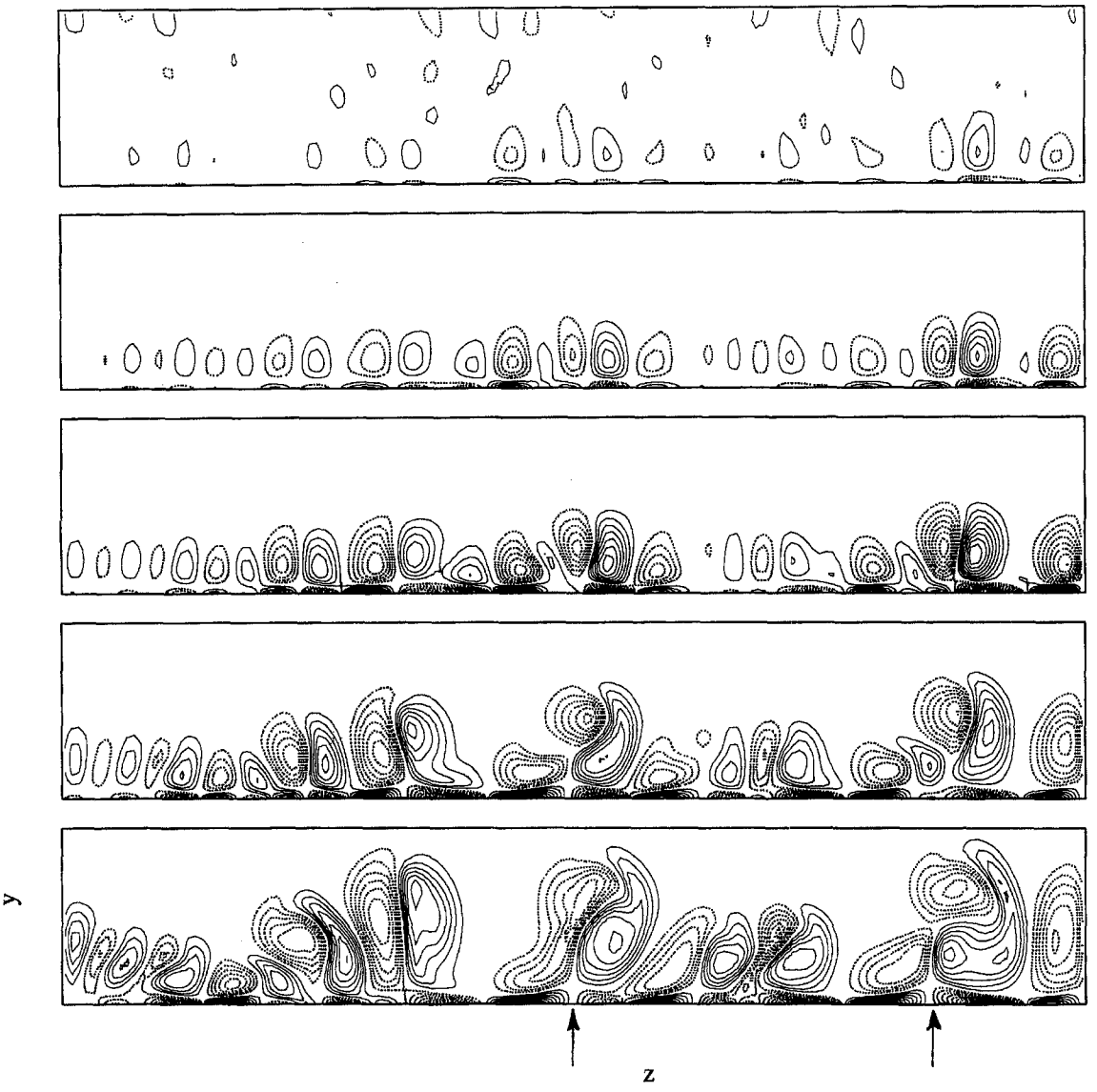

Figure 17. Streamwise vorticity field in the cross section at the same x values as Figure 15, $Ro = 0.3$. Isolines spacings are 0.3 (for $x = 1.6$), 0.6 ($x = 2$), 1.2 ($x = 2.4$), and 2 ($x = 2.8$, 3.2); zero lines are not drawn.

Table 1

	$x = 2$			$x = 2.4$			$x = 2.8$			$x = 3.2$		
Ro	−0.3	0	0.3	−0.3	0	0.3	−0.3	0	0.3	−0.3	0	0.3
Number of cells		10	13	8	9	12	8	9	11	8	9	10
Λ		181	125	250	212	138	250	212	157	250	212	181
λ^+		84	66	100	92	86	97	104	122	96	130	144
y_c^+		26	24	34	29	39	34	38	49	35	57	75
η_c		1.98	1.77	2.45	2.00	2.20	2.33	2.15	1.97	2.23	2.35	2.63

extensive parametric studies, including, in particular, receptivity calculations. Nonparallel linear approximation ceases to be valid at the stage where the vortices develop their typical "mushroom" shape, and the perturbation energy then saturates and remains at a nearly constant level, which depends on the wavelength but not on Ro. Our calculations show that the energy density E/E_0 grows with Λ.

In this paper it is shown how positive rotation enhances the development of the vortices while negative rotation retards their spatial development. For $Ro = 0$, the linearly most amplified wavelength was found to be close to $\Lambda = 200$, in agreement with previous experimental and numerical results. It decreases with positive Ro, and increases when Ro is negative (consistent with experimental evidence by Matsubara and Masuda (1991) for the rotating flat-plate boundary layer). However, wavelength selection is weak when the instability is weak, i.e., at low G and negative Ro. This may explain why widely varying wave numbers have been obtained in different experiments. In an experiment the spanwise distance between neighboring vortices can be forced by the upstream field or imposed conditions, or can be allowed to form naturally. We have performed numerical experiments to study the natural formation of steady Görtler vortices in a long (along the span) box, subject to random inlet perturbation fields. Initially, the flow fields go through a linear receptivity phase which selects the modes to be amplified *independently of the initial perturbation amplitude level.* However, different inflow random noise distributions yield different vortical structures downstream, but approximately the *same average wavelengths.* This indicates that the initial filtering phase is similar for different initial conditions. The natural average wavelengths obtained are very close to those predicted by linear analysis. As the vortices develop into the strongly nonlinear stage, the wavelength increases due to merging of the most narrowly spaced vortices, a process related to Eckhaus instability. This is seen most clearly at positive Ro, for which the nonlinear development of the vortices is enhanced. Interestingly, the characteristic dimensions of the vortices scaled in viscous (wall) units are in the range of those found in turbulent boundary layers.

The conclusions of this numerical study should be relevant to future experiments on the rotating Görtler problem. Some such experiments are currenly being carried out at EPF Lausanne. In this paper we have shown how sensitive the system is to initial perturbations. Therefore, it is of utmost importance to document the inlet conditions carefully. If these cannot be properly defined, it is preferable to trigger the vortices at the entrance of the test section in a controlled fashion. Because of the different growth rate and saturation levels of vortices with different Λ's, it may also be possible to tailor the streamwise variation of wall skin friction and the onset of secondary instabilities and transition to specific applications such as flow over turbine blades.

Acknowledgments

We would like to thank Professor I.L. Ryhming for initiating this collaborative effort, Professors T. Maxworthy and V. Sabelnikov for several interesting discussions, and Professor P.A. Monkewitz for reading the original manuscript and for comments that led to Figure 16.

Appendix

The elements of the two-dimensional matrix operators in y defining the linear problem are:

$$L_{11} = -(D^2-\alpha^2)^2 + V(D^2-\alpha^2)D + V_y(D^2-\alpha^2) + \sigma U(D^2-\alpha^2) + V_{yy}D + V_{yyy} - \sigma U_{yy},$$

$$L_{12} = -V_x(D^2+\alpha^2) - 2\alpha^2 G^2(U+Ro) + 2\sigma(V_y D + V_{yy}) + V_{xyy},$$

$$L_{21} = U_y,$$

$$L_{22} = -(D^2-\alpha^2) + \sigma U - V_y + VD,$$

$$M_{11} = U(D^2-\alpha^2) - U_{yy},$$

$$M_{12} = 2(V_y D + V_{yy}),$$

$$M_{21} = 0,$$

$$M_{22} = U,$$

where D denotes $\partial/\partial y$.

References

Aouidef, A., Wesfreid, J.E., and Mutabazi I. (1992) Coriolis effects on Görtler vortices in the boundary-layer flow on concave wall. *AIAA J.* **30**, 2779.

Bertolotti, F.P. (1991) Linear and Nonlinear Stability of Boundary Layers with Streamwise Varying Properties. Ph.D. Thesis, The Ohio State University.

Bertolotti, F.P., Herbert, T., and Spalart, P.R. (1992) Linear and nonlinear stability of the Blasius boundary layer. *J. Fluid Mech.* **242**, 441.

Bippes, H. (1978) Experimental study of the laminar-turbulent transition of a concave wall in a parallel flow. NASA TM 75243.

Bippes, H., and Görtler, H. (1972) Dreidimensionale Störungen in der Grenzschicht an einer konkaven Wand. *Acta Mech.* **14**, 251.

Blackwelder, R.F. (1983) Analogies between transitional and turbulent boundary layers. *Phys. Fluids* **26**, 2807.

Bottaro, A. (1993) On longitudinal vortices in curved channel flow. *J. Fluid Mech.* **251**, 627.

Bottaro, A., and Klingmann, B.G.B. (1996) On the linear breakdown of Görtler vortices. *European J. Mech. B/Fluids*, in press.

Butler, K.M., and Farrel, B.F. (1992) Thre-dimensional optimal perturbations in viscous shear flows. *Phys. Fluids A* **4**, 1637.

Day, H.P., Herbert, T., and Saric, W.S. (1990) Comparing local and marching analyses of Görtler instability. *AIAA J.* **28**, 1010.

Eckhaus, W. (1965) *Studies in Non-Linear Stability Theory*. Springer Tracts in Natural Philosophy, Vol. 6. Berlin: Springer-Verlag.

Floryan, J.M., and Saric, W.S. (1984) Wavelength selection and the growth of Görtler vortices. *AIAA J.* **22**, 1529.

Guo, Y. (1992) Spanwise Secondary Instability of Dean and Görtler Vortices. Ph.D. Thesis, University of Alberta.

Guo, Y., and Finlay, W.H. (1994) Wavenumber selection and irregularity of spatially developing nonlinear Dean and Görtler vortices. *J. Fluid Mech.* **264**, 1.

Hall, P. (1983) The linear development of Görtler vortices in growing boundary layers. *J. Fluid Mech.* **130**, 41.

Klingmann, B.G.B. (1993) Linear Parabolic Stability Equations Applied to Three-Dimensional Perturbations in a Boundary Layer. Report T-93-12, IMHEF-DME, Swiss Federal Institute of Technology, Lausanne.

Kristoffersen, R., and Andersson, H.I. (1993) Direct simulations of low-Reynolds number turbulent flow in a rotating channel. *J. Fluid Mech.* **256**, 163.

Landahl, M.T. (1980) A note on an algebraic instability of inviscid parallel shear flows. *J. Fluid Mech.* **98**, 243.

Lee, K., and Liu, J.T.C. (1992) On the growth of mushroomlike structures in nonlinear spatially developing Goertler vortex flow. *Phys. Fluids A* **4**, 95.

Malik, M.R., Li, F., and Chang, C.-L. (1994) Cross-flow disturbances in three-dimensional boundary layers: nonlinear development, wave interaction and secondary instability. *J. Fluid Mech.* **268**, 1.

Matsson, O.J.E., and Alfredsson, P.H. (1990) Curvature- and rotation-induced instabilities in channel flow. *J. Fluid Mech.* **210**, 537.

Matsson, O.J.E., and Alfredsson, P.H. (1994) The effect of spanwise system rotation on Dean vortices. *J. Fluid Mech.* **274**, 243.

Matsubara, M., and Masuda, S. (1991) Three dimensional instability in rotating boundary layer. In *Boundary Layer Stability and Transition to Turbulence* (D.C. Reda, H.L. Reed, and R. Kobayashi, eds.). FED, Vol. 114, p. 103 New York: ASME.

Patankar, S.V., and Spalding, D.B. (1972) A calculation procedure for heat, mass and momentum transfer in three-dimensional parabolic flows. *Internat. J. Heat Mass Transfer* **15**, 1787.

Pexieder, A., Truong, T.V., Maxworthy, T., Matsson, J.O.E., and Alfredsson, P.H. (1993) Görtler vortices with system rotation: experimental results. In *Spatio-Temporal Properties of Centrifugal Instabilities*. NATO Advanced Research Workshop, Nice, March 28–29, 1993.

Potter, M.C., and Chawla, M.D. (1971) Stability of boundary layer flow subject to rotation. *Phys. Fluids* **14**, 2278.

Robinson, S.K. (1991) Coherent motions in the turbulent boundary layer. *Annual Rev. Fluid Mech.* **23**, 601.

Swearingen, J.D., and Blackwelder, R.F. (1986) Spacing of streamwise vortices on concave walls. *AIAA J.* **24**, 1706.

Swearingen, J.D., and Blackwelder, R.F. (1987) The growth and breakdown of streamwise vortices in the presence of a wall. *J. Fluid Mech.* **182**, 255.

Tani, I. (1962) Production of longitudinal vortices in the boundary layer along a curved wall. *J. Geophys. Res.* **67**, 3075.

Trefethen, L.N., Trefethen, A.E., Reddy, S.C., and Driscoll, T.A. (1993) Hydrodynamic stability without eigenvalues. *Science* **261**, 578.

Yanase, S., Flores, C., Métais, O., and Riley, J.J. (1993) Rotating free-shear flows. I. Linear stability analysis. *Phys. Fluids A* **5**, 2725.

Zebib, A., and Bottaro, A. (1993) Goertler vortices with system rotation: Linear theory. *Phys. Fluids A* **5**, 1206.